Journal of the Meteorological Society of Japan

EARLY ONLINE RELEASE

The DOI for this manuscript is
DOI:10.2151/jmsj.2021-030
J-STAGE Advance published date: February 24th, 2021
The final manuscript after publication will replace the preliminary version at the above DOI once it is available.

Retrieval of attenuation profiles from the GPM dual-frequency radar observations

Takahisa Kobayashi[1,2] , Mitsuharu Nomura[1] ,Ahoro Adachi[2],

Soichiro Sugimoto[1], Nobuhiro, Takahashi[3],and Hiromaru Hirakuchi[1].

[1]*Central Research Institute of Electric Power Industry,1646, Abiko, Chiba, Japan, 270-1194*

[2]*Meteorological Research Institute, Tsukuba, Japan, 305-0035*

[3]*Nagoya University, Nagoya, Japan,464-8601*

Jan. 5, 2021

----

1) Corresponding author: Takahisa Kobayashi

Central Research Institute of Electric Power Industry/Meteorological Research Institute

1646 Abiko, Abiko-shi,Chiba 270-1194 JAPAN.

Email: kobay@mri-jma.go.jp

Tel: +81-3-3216-4403

Fax: +81-4-7184-7142

Abstract

A new method that retrieves attenuation profiles using a Dual-Frequency Precipitation Radar (DPR) equipped on the Global Precipitation Mission (GPM) is proposed. The DPR operates at Ka and Ku-bands and provides profiles of a differential frequency ratio , which is the difference of the measured or attenuated reflectivity in decibel scale between Ka and Ku bands. For accurate measurements of precipitation, hydrometeor classification is essential. Attenuation of radio wave due to precipitation is closely related to microphysical properties and available for hydrometeor classification. The proposed method estimates range variations of relative values of differential attenuation between two frequencies and can be used for identifying hydrometeor types along the radar propagation path. Numerical simulations indicate that the proposed method performs well for rain, melted snow, mixed-phase precipitation, and some cases of the melting layer. The method was also evaluated for GPM DPR measurements. Results indicate that the method works well for identifying rain and snow and also provides useful information for melting layer detection and attenuation, even for the melting layer in which no enhancement of reflectivity is observed.

Keywords GPM, DPR, attenuation, hydrometeor classification

1. Introduction

A Dual-Frequency Precipitation Radar (DPR) equipped on the Global Precipitation Mission (GPM) core satellite operates at Ku- and Ka-band frequencies and has a potential to measure more accurate rainfall rates (e.g., Akiyama et al., 2019, Liao and Meneghini, 2020, Seto et al., 2021) than the space-borne Precipitation Radar (PR) operated at a single frequency on the Tropical Rainfall Measuring Mission (TRMM) satellite. Furthermore, the GPM core satellite measures higher latitude regions than the TRMM satellite and can measure snow for wide regions. Accurate snow measurement is one of critical topics to be solved in radar meteorology. The relationship between the radar reflectivity (Z) and snowfall rate (s) differs significantly from the relationships for rain (Z-R relations). Furthermore, the Z-s relationship varies significantly with snow type, e.g., dry snow, wet snow, and mixed-phase precipitation. Therefore, hydrometeor classification is, as a first step, needed for quantitative precipitation estimation from the Z-R(s) relationship.

Traditionally, snow regions have been identified from the ambient temperature and relative humidity (e.g., Matsuo and Sasyo, 1981). For dual-polarization radars, many hydrometeor classification methods have also been developed (e.g., Kouketsu et al., 2015, Chandrasekar et al., 2013, Kobayashi et al., 2017). The DPR is a single-polarization radar operated at 35 and 14 GHz. In DPR measurements, identifying snow areas was done using the ambient temperature and relative humidity and a microwave imager (e.g., Skofronick-Jackson et al., 2019). Another approach for DPR is using the difference of the measured reflectivities at Ka and Ku bands which is called, the differential frequency ratio (DFR). For non-attenuating media, DFR is defined as the logarithmic difference between the equivalent radar reflectivity factor (Z_e) at Ku and Ka bands as

$$DFR = Z_e(Ku) - Z_e(Ka). \qquad (1)$$

Precipitation of the non-Rayleigh and Rayleigh regime of scattering for Ka and Ku bands, respectively, produces DFR. Increases in DFR generally, appear for precipitation of larger particles (e.g. Le and Chandrasekar, 2013, 2016). For attenuating media, DFR arises from different scattering and attenuation properties between two frequencies and is expressed as

$$DFR = DFR_m = Z_m(Ku) - Z_m(Ka), \qquad (2)$$

where DFR_m is the measured DFR and Z_m is the measured radar reflectivity. In the absence of attenuation, DFR can be an indicator of snowflake size (Matrosov, 1998) and discriminate snow and rain from the DFR-Z_m(Ku) relationship (Liao and Meneghini, 2011). Snow density can also be identified from the relationship. In the presence of attenuation, these techniques need accurate attenuation correction. Hereafter, the DFR is used as the logarithmic difference in the measured (apparent) radar reflectivity factor between Ku and Ka bands.

For reflectivity-based rainfall rate estimates, attenuation is an amount to be removed from radar received signals. Many extensive studies have been conducted for attenuation correction to estimate accurate rainfall rates. For DPR, the surface reference technique has been applied for attenuation correction. The attenuation-based approach has also been developed for rainfall rate estimation (Matrosov, 2005, Ryzhkov, et al., 2014). Attenuation is useful for rainfall estimation because it is closely related to rainfall rates, i.e., the sensitivity of the attenuation-rainfall rate relation to the variation of drop size distribution (DSD) is lower than Z_e. Although specific attenuation is relatively insensitive to DSD, it depends on the type of precipitation. Dry snow attenuation is generally small at most radar frequencies, whereas for rain, large attenuation appears depending on DSD and rain rate. Some melting hails have large attenuation (Thurai et al., 2015). In other words, attenuation is useful for hydrometeor classification. Attenuation-based hydrometeor classification, therefore, is considered possible (Kobayashi et al., 2015, 2017).

No straightforward methods exist for accurate attenuation estimation. Most methods to estimate attenuation use redundancy relations among radar observables (Adachi et al., 2015). Specific attenuation(SA) can be estimated if SA is related to the radar reflectivity factor by a power law (Hitshchfeld and Bordan,1954). This method was modified using path-integrated attenuation, which was used in the rainfall rate estimations algorithm in the PR algorithm (Meneghini and Nakamura, 1990, Iguchi and Meneneghini, 1994). This method was further modified for the DPR algorithm (Meneghini et al., 2021).

In this study, we propose a new method for attenuation estimation from the spatial variability of the measured reflectivity in the radar propagation path instead of the variables at each radar resolution volume. DPR observations show that measured DFR often tends to increase toward downward because larger attenuation of the radio wave in rain, in general, occurs at higher radar frequencies. The proposed method uses DFR to estimate range variations of relative values of attenuation for hydrometeor classification.

2. Method for attenuation estimation from the DFR (D-MAD)

The DPR onboard the GPM core satellite operates at frequencies of Ka-band (35 GHz) and Ku-band (14 GHz). For small raindrops, the scattering properties at both Ka and Ku-band radars are almost in the Rayleigh regime, resulting in small DFR_m values, unless attenuation is significant. For large raindrops, the scattering properties at the Ka-band radar are in the Mie regime but still in the Rayleigh regime at the Ku-band radar, resulting in larger DFR_m values. For snow, on the other hand, the scattering properties are in the Mie regime for both Ka and Ku-band radars. Larger particles generally lead to larger DFR_m values. DFR arises from the different scattering properties of particles between Ka and Ku-bands is called here as 'scattering effect (DFR_s)'.

In addition to the scattering effects, different specific attenuation between Ka and Ku bands increases the DFR_m. Larger attenuation of the radio wave in precipitation, in general, occurs at higher frequencies. The increase in DFR_m due to attenuation is determined from the differential attenuation between Ka and Ku-bands and is defined here as 'attenuation effects (*δA*'. The *δA* is given by

$$\delta A = A(Ka,r) - A(Ku,r), \tag{3}$$

where *A*(Ka,*r*) and *A*(Ku,*r*) are the two-way path attenuation to the range *r* at Ka and

Ku-bands.

For rain, DFR_m is determined by both the scattering and attenuation effects. For dry snow, DFR_m is determined by only the scattering effects because attenuation is almost negligible at both 35 and 14 GHz.

$$DFR_m = DFR_s + \delta A \ , \qquad \text{for rain.} \tag{4}$$

$$DFR_m = DFR_s, \qquad \text{for dry snow.}$$

If the δA is detected in the measured DFR, precipitation is identified as rain. This method has advantages that no accurate attenuation correction is needed.

Figure 1 shows range variations of measured reflectivities, Z_m(Ka) and Z_m(Ku), for snow and rain conditions. For snow, DFR_m is determined from the scattering effects, as in Eq. (4). There is no apparent shape of DFR_m with the radar range. For rain, Z_m(Ka) continues decreasing below the height of bin no. 150 associated with its significant attenuation. Because Z_m(Ku) remains almost constant below bin no. of 150, DFR_m is almost determined by δA and tends to increase with the radar range. For attenuating medium, such as intense rain, DFR_m monotonically increases with the radar path length if DFR_s remains constant, whereas, for dry snow, no such apparent increases in DFR_m are observed. We can use the range variations in DFR_m as a basis for discriminating rain from snow.

The range variations of DFR_m, however, are determined from the scattering and attenuation effects. A key factor for hydrometeor classification, therefore, is how to estimate the attenuation effects in DFR_m. To detect δA, DFR_s should be removed from DFR_m. The scattering effects are basically related to the particle sizes. Large values of DFR_s arise primarily from large particles. Intense rain is generally associated with large particles, i.e., larger reflectivity values at the Ku-band. Therefore, the DFR_s can be expected to increase with the intrinsic value of the reflectivity. Here, DFR_s in linear scale (DFR_{sL}) is assumed to be related to Z_e(Ku) in linear scale (Z_{eL}) by a power law as

$$DFR_{sL} = cZe_L{}^d. \tag{5}$$

The coefficients *c* and *d* depend on precipitation type. We assume that Z_e(Ku) can be approximated as the measured value Z_m at the Ku-band. Then, the δA can be given by

$$\delta A = DFR_m - 10\,log\,c - dZ_m(Ku) = Dz - 10\,log\,c\,, \tag{6}$$

where

$$Dz \equiv DFR_m - dZ_m(Ku). \tag{7}$$

The variables in Eqs. (6) and (7) are in logarithmic scale. Given that the coefficient *c* is assumed to be constant in the small range of *dr*, the derivative of δA regarding the range is given as

$$\frac{d\delta A}{dr} = \frac{dDz}{dr} - 10\frac{d\,log\,c}{dr} \approx \frac{dDz}{dr}. \tag{8}$$

As shown in Eq. (3), δA is the difference of A(Ka,r) and A(Ku,r), which are the two-way path attenuation to range *r*, i.e., twice the integrated values of the specific attenuations from the radar range 0–*r*, at Ka and Ku-bands. Therefore, the derivative of δA regarding range gives twice the difference of the specific attenuation and is referred to here as the differential frequency attenuation (DFA). The parameter Dz, therefore, is a DFA measure. The value obtained by Eq. (8) is proportional to DFA. The method to estimate DFA from DFR_m is referred to as the Dual-frequency Method for Attenuation Difference (D-MAD) between two frequencies. This method obtains range variations of the relative DFA values from the DPR measurements.

In the method, DFR_s calculated from Eq. (5) is used to obtain δA by subtracting DFR_s from DFR_m. Since such calculated DFR_s is different from the true DFR_s value, depending on the properties of precipitation, the DFA estimated from the δA is different from the true DFA value. This method, therefore, cannot give the exact DFA values; however, it can give relative or qualitative DFA variations with radar path if the estimated values of Dz are linearly related to δA.

The key point of D-MAD lies in the assumption of Eq. (5). The dual-frequency ratio associated with the scattering effect tends to increase with the size of hydrometeors. When precipitation particles fall, their sizes change, resulting in the variability of DFR_s in the radar path. To consider the variability, the DFR_s-Z_e relationship by Eq. (5) is used. Figure 2 shows simulated Dz versus theoretical values of $A(\mathrm{Ka},r)$-$A(\mathrm{Ku},r)$ for (a) rain and (b) melting snow. The rain rate varies from 0 to 50 $\mathrm{mmh^{-1}}$, with the radar range and size of raindrops vary according to the Marshall-Palmer (M-P) DSD. Although variabilities of raindrop sizes exist in the radar path, Dz is linearly related to δA, indicating that Eq. (5) can accurately provide DFR_s. For snow, the water fraction of snow changes from 0 to 1 with range (Fig. 2b), resulting in the variability of the size of snow particles. Snow density above the melting level was 0.06 gcm^{-3}. The DSD is expressed by a three-parameter Gamma function as

$$N(D_m) = N_0 D_m^{\mu} \, exp(-\Lambda D_m), \qquad (9)$$

where, D_m is a major axis of snow particles. The shape parameter μ was assumed to be 3. The slope parameter Λ (mm^{-1}) is related to the mean volume equivalent diameter (D_0) and is taken to be 3.33 in the calculations. The Dz values are almost linearly related with δA, except at the boundary of the melting and rain layers. Although the absolute Dz values are different from theoretical values, the range variation of the estimated DFA values could be similar to the theoretical values associated with the linear relationships between Dz calculated with Eq. (5) and the theoretical values. The range variations of the estimated DFA are similar to the theoretical values for rain (Fig. 3a) and melting snow (Fig. 3b). The DFA peak altitudes are slightly higher than the theoretical values, which could be due to attenuation in Z_m(Ku). The coefficient of *d* was taken to be 0.3 for rain and 0.1 for snow, which were selected as the Dz monotonically increases with radar range.

The Dz values are linearly related with δA for rain but are less linearly related for melting snow (Fig. 2). In actual melting processes, the relationship could be worse because of significant and rapid changes in the water fraction of snow, size, and concentrations. Thus, large DFR_s variabilities could occur in the actual melting layer, where DFR_s could be insufficiently given by Eq. (5). For the melting layer, specifically for stratiform in which reflectivity enhancement appears, we added a term δDFR_s and modified Eq. (5) as

$$DFR_s(ML) = DFR_s(w_1 + w_2 \delta DFR_s), \tag{10}$$

in logarithmic scale, where w_1 and w_2 are weights. The term δDFR_s is introduced to correct discrepancies of DFR_s given by Eq. (5) in the melting layer. Section 4 provides a detailed explanation of δDFR_s.

Note that the method gives the range variation of relative DFA values, which has no unit, with a radar propagation path. Hereafter, we use attenuation as DFA because attenuation at the Ku-band is almost negligible. Note again that the estimated DFA is not the actual DFA value but a relative value when the correct values of the coefficient *d* are unknown.

3. Sensitivity of DFR_s-Z relations to attenuation estimation

To remove DFR_s from DFR_m, the DFR_{sL}-Z_{eL} relationship is assumed as in Eq. (5). This relationship corresponds to the relationship $Z_{eL}(Ka)=Z_{eL}(Ku)^{(1-d)}/c$. The coefficients, therefore, depend primarily on particle size for rain (Liao and Meneghini, 2005, Matrosov,2005). For snow, the coefficients also depend on the density, shape, and particle size (Petty and Huang, 2010, Liao and Meneghini, 2011). This relationship is reasonable for larger values of $Z_e(Ku)$, even for aggregate snow (Kobayashi et al., 2018). The coefficient *c* in Eq. (5) is an intercept parameter of the relationship between reflectivities at the two frequencies and is primarily related to DSD (Kuo et al., 2004). The large variability of the coefficient appears to be associated with the large variability of DSD in the radar path. The coefficient *c* variations in the radar range lead to bias in the estimate. The coefficient could be less variable for a narrow range to calculate the differential change. Furthermore, the bias would be compensated to some degree if Z_e (or DFR_s) is well correlated to δA, i.e., fewer effects of the variability on $d\delta A/dr$.

For precipitation of the Rayleigh scattering regime at both frequencies, $d = 0$. For precipitation of the Mie scattering regime at both frequencies, DFR increases with the raindrop size. Fortunately, the coefficient *d* is not sensitive to the size (Liao and Meneghini,2005, Kuo et al., 2004). The coefficient also depends on the snow density because the refractive index of snow depends on snow density. The coefficient *d*, however, does not change significantly, except for small values of DFR_s and Z_e(Ku).

The variability of the coefficients was examined by making DPR simulations for rain, snow, and mixed precipitation of rain and ice particles and evaluating the sensitivity of the DFR_s-Z_e relationship to the estimated δA and DFA. Figure 4 shows DFR_s-Z_e(Ku) relationships for (a) rain and (b) melting snow. For rain, DFR_s is almost linearly related to Z_e(Ku) in dB unit for thunderstorms, drizzle (Joss and Waldvogel, 1969, Oguchi,1983), and rain of M-P type DSD (Marshall and Palmer,1948). Raindrop shapes are assumed to be oblate, and the axis ratio varies with the drop size (Beard and Chung, 1987). Although the intercept parameter *c* varies significantly associated with DSD variability, the slope parameters *d* are almost identical for three DSD types.

Figure 4b plots the relationships for various values of liquid water fraction of melting snow. The snow particle shape was assumed to be oblate, and the axis ratio was assumed to be constant at 0.66 (Matrosov 2008). Fisher probability density was used for oriention the symmetry axis of snow particles. The DSD by Gunn and Marshall (1948) was applied. The snow model used in this study is the so called soft oblate model. We assumed snow as a uniform mixture of ice, air, and water and calculate the refractive index of snow particles using the Maxwell-Garnet (1904) (M-G) theorem for various fractions of water in snow. These calculations might agree with the results of complicated snow particle shapes (Liao et al., 2016). Mass of snow, *M* can be related to the size of snow (*D*) and is given by

$$M = eD^{f}. \tag{11}$$

The coefficients *e* and *f* were given by Heymsfield et al. (2004). The snow temperature was assumed to be constant at 270 K. For melting snow, DFR_s is also linearly related to Z_e(Ku), except for small values of DFR_s in which attenuation is generally small. The slope parameter *d* is almost independent of the liquid water fraction in snow.

The sensitivity of DFR_s-Z_e relations to the estimated DFA was also examined using simulations for rain, snow, and mixed-phase precipitation. Figure 5 shows vertical profiles of the parameter (a) Dz and (b) estimated DFA for rain. The rainfall rate is assumed to vary in Gaussian with altitude. The rain rate is a maximum of 20 mmh^{-1} at an altitude of 5 km. These range variations could be unrealistic for DPR measurements but are used to examine the method under strict conditions. The Gaussian variations where the rain rate changes with low, high, and low altitudes result in significant changes in DFA and are suitable for validating the method. The temperature was assumed to be constant to examine the dependence of the error on the radar range. Various Dz values of the coefficient *d* are plotted. Similar behavior of Dz with altitude are obtained for various values of the coefficient *d*. Accordingly, the range variations of DFA estimated from dDz/d*r* are less sensitive to the variation of the coefficients *d* and correlate well with the shape of range variation of the theoretical values. An optimum value of *d* was selected, as Dz increases monotonically with the radar range. Note that the method shapes (relative spatial variability) the range variations of the relative values of DFA; peak ranges are consistent with the theoretical one but the peak values are different.

Figure 6 is the same as Fig. 5, except for melting snow. The volume fraction of liquid water of melting snow changes in Gaussian with altitude and is a maximum value of 0.2 at an altitude of 5 km. This situation might not be realistic but is suitable for the sensitivity study, as in Fig. 5. The DSD ($N(D)$) expressed by a three-parameter Gamma function (Eq. (9)) was applied. The results for various values of the coefficient *d* are also plotted. Range variations of Dz are almost independent of the coefficient *d*. Accordingly, DFA range variations are less sensitive to the variation of the coefficients *d* and correlate well with the variation of the theoretical attenuation.

Figure 7 shows estimated DFA for mixed-phase precipitation where snow and rain coexist. The volume fraction of rain in the mixed-phase precipitation increases from 0 to 1 linearly with altitude from the top to the bottom of precipitation. The total liquid (ice) water content is constant for the entire range. The estimated attenuation is almost insensitive to the coefficient *d* and is consistent with the theoretical attenuation.

4. Application to the Melting layer

As mentioned earlier, the key point of the method lies in the DFR_s-Z_e relationship. The assumption of Eq. (5) is appropriate for precipitation of no significant changes in the microphysical properties (Section 3). In the melting layer (ML), however, the large variability of the radar reflectivity associated with the variability of the microphysical properties might exist. The transition from the solid to the liquid phase precipitation might result in variability of DFR_s-Z_e relations in ML, resulting in some error in the estimated DFA. In this section, we examine the applicability of D-MAD in the ML.

Precipitation is usually classified into convective and stratiform types. For convective precipitation, no significant enhancement of the radar reflectivity usually appears near the ML, making it challenging to detect ML from the vertical profiles of the reflectivity. ML detection is essential for accurate measurements of rainfall rates from the DPR. Although the reflectivity does not change significantly in ML, attenuation is expected to change discontinuously at the top and bottom of the ML boundaries because the differences of the imaginary part of the refractive index between ice and water are larger than those of the real part of the refractive index (Oguchi, 1983). Mixed-phase precipitation in which liquid and solid phases coexist also results in no significant radar reflectivity enhancement and a slight change in DFR_s-Z_e relations in the radar range. Fortunately, this condition is suitable for D-MAD. Thus, the ML could be detected if there are discontinuities in the estimated attenuation at the top and bottom of ML, even for precipitation in which a bright band (BB) is not observed. Note, here we do not intend to develop a method to detect ML but examine the applicability of the method in the ML.

For stratiform precipitation, a clear BB is often observed in ML, making it possible to detect ML from the vertical profiles of the reflectivity. Although no attenuation estimate is needed to detect ML in this case, attenuation estimation in ML is needed for accurate rainfall estimates and essential for a better understanding of the microphysical properties of precipitation (Klaassen, 1990). The enhancement magnitude of the radar reflectivity and DFR_m in the ML depends on the snow densities above ML.

As discussed in Section 2, DFR_s tends to be larger for larger particles. When low-density snow melts, large melting snow particles increase DFR_s and the reflectivity enhancement. As the snow particles melt further, the particle sizes decrease, rapidly decreasing DFR_s. The degree to which DFR_s increases/decreases with Z_e differs, depending on the microphysical properties of snow. Figure 8a shows simulated DFR_s and Z_e(Ku) range variations of melting snow in the ML. Water fractions of snow are 0 at an altitude of 2.1 km and 1 at 1.1 km. The density of the snow above ML is 0.1 gcm^{-3}. The reflectivity increases sharply from the top of the ML and becomes maximum at ~1.6 km. DFR_s increases slowly from the top of the ML and decreases more rapidly below 1.6 km than that of Z_e(Ku), indicating different DFR_s-Z_e relations above and below the altitude of the maximum Z_e(Ku), depending on the microphysical property profiles. The altitude of the local maximum of the DFR_s is higher than that of Z_e(Ku). Figure 8b shows scatter plots of the range variations of Z_m(Ka), Z_m(Ku), and DFR_m. Data were collected from the GPM DPR observation on 7 July, 2018. Similar variations of Z_m(Ku) and DFR_m are shown. The maximum DFR_m ranges are, however, smaller (higher altitude) than Z_m(Ku).

To consider the variability of the DFR_s-Z_m(Ku) relationships in ML, as mentioned in (Eq. (10)), we modify Eq. (5) as

$$DFR_s = w_1 dZ_m(Ku) + w_2 dZm(Ku)\delta DFR_s, \qquad (12)$$

in logarithmic scale. Coefficients w_1 and w_2 are weights. The first term of the right side corresponds to Eq. (5). The term δDFR_s is introduced to correct the asymmetric variability of the DFR_s-Z_e relation in ML. The three-parameter Gamma function is applied to δDFR_s in Eq. (12) as

$$\delta DFR_s = N_m r_m^{\mu} \, exp(-\Lambda_m r_m), \qquad (13)$$

where r_m is a length from the bottom of ML. Λ_m is defined from μ and the range of the local maximum of Z_m(Ku) (r_{max}), as $\Lambda_m = \mu / r_{max}$. Here, μ was taken to be 2. N_m is a normalized factor. Note that this term is sensitive to the range of the bottom of the ML (r_{mlbot}) determined from the reflectivity profiles. When the bottom of the ML is unclear, r_{mlbot} was determined so that δDFR_s is small enough (0.1–0.2) at the top of the ML.

Figure 9a shows simulated profiles of DFR_s and Dz for melting snow. Snow starts melting at an altitude of 2 km and becomes rain at 1 km. The vertical profiles of apparent (measured) reflectivity Z_{Ka}, Z_{Ku}, and DFR are also shown (upper axis). Slight decreases in the non-modified Dz (Dz1, Eq. (7)) appear in the middle of the ML. However, the modified Dz (Dz2) increases monotonically with a radar range below 2 km. The decreasing tendency of Dz2 above ML is because of the excess values of δDFR_s. Narrower δDFR_s is appropriate. As shown in Eq. (12), DFR_s is the sum of DFR_s1 (the first term of Eq. (12)) and the correction term (second term of Eq. (12): DFR_s2) and has a large peak at an altitude of 1.75 km, indicating a large scattering of melting snow at the Ku-band. The vertical profile of DFR_s is similar to the theoretical profile of DFRs. Here, w_1 is applied as 0.4 and w_2 is 0.6.

In using Eq. (12), the question is how to determine the weight. Figure 9b shows Dz and DFA for various weight values. The notation 2w19 represents $w_1 = 0.1$, $w_2 = 0.9$, 2w28 is $w_1 = 0.2$, $w_2 = 0.8$, and 2w37 is $w_1 = 0.3$ and $w_2 = 0.7$. The notation 1w0 means no corrected Dz. The Dzw37 profile is not plotted because it is similar to Dz28. For DFA1w0 and DFA2w19, the DFA peak unrealistically appears above the ML, but the peaks for DFA2w28 and DFA2w37 are near 1.7 km, correlating with the theoretical profile of the differential specific attenuation between Ka and Ku-bands. If δDFR_s, is set in the correct ML region, the weight effects might not be so significant for many ML cases. More studies, however, are needed to determine appropriate weight values.

To evaluate the DFR_s-Z_e relationship using Eq. (12) in the estimated DFA, we applied the D-MAD to the data measured using GPM at Shikoku, Japan on 7 July, 2018. To examine the applicability in detail, data of three types of range variations of Z_m and DFR_m were selected. Here we refer to convective precipitation as Type 1, where no enhancement occurs in both Z_m(Ku) and DFR_m in the ML. We separated stratiform into two types. One is Type 2, where reflectivity enhancement appears, but no DFR_m enhancement appears in ML. These profiles are often seen in GPM measurements. The other is Type 3, where significant enhancement was observed in both Z_m(Ku) and DFR_m. In the estimate, the measured Z_m(Ku) and DFR_m values were smoothed using the locally weighted regression (Cleveland, 1979). If the smoothing is insufficient, Dz was furthermore smoothed. The parameter specifying the smoothing amount was taken to be 0.2–0.5. The derivative over the three range bins each was taken.

Figure 10 shows the vertical profiles of Z_m(Ka), Z_m(Ku), DFR_m, and estimated DFA based on the DFR_s-Z_e relationship using Eq. (5) (DFA1) and Eq. (12) (DFA2) for data selected from Type 1 precipitations. In Type 1, DFR_m increases monotonically with the radar range, indicating no significant range variability in the DFR_s-Z_e relationship. The large weight values of w_1 = 0.75 and small values of w_2 = 0.25 were adopted. Therefore, DFA1 is similar to DFA2 (Fig. 10a, b). Some differences exist between DFA1 and DFA2 (Fig. 10c, d). In Fig. 10 (a, b), DFR_s is almost constant near the top of the ML. On the other hand, DFR_s increases in Fig. 10(c, d). The DFR_s-Z_e relations might be more sufficiently given by Eq. (12) than Eq. (5). In Fig.10b, Z_m(Ka) decreases below ML (3–4 km), whereas Z_m(Ku) remains almost constant, monotonically increasing DFR_m, indicating large attenuation in and below the ML, as indicated by DFA. No apparent BBs are observed in Type 1, making it challenging to detect the ML from the reflectivity profiles. Attenuation estimation using D-MAD could be useful to detect the ML. In Fig. 10(c, d), Z_m(Ka) and DFR_m remain almost constant in the altitude from 2 to 4 km, indicating precipitation of small attenuation in this range.

The method was shown to apply to ML detection of convective precipitation from distinct attenuation profiles. To confirm the applicability of the technique for the ML, simulations were made for ML similar to Type 1. In Type1, DFR_m continuously increases from the top of ML to the ground, whereas Z_m(Ku) remains almost constant. Melting ice particles, such as graupel, produce similar profiles (Zawadzki et al.,2005). Figure 11 shows the simulated vertical profiles of Z_{Ka}, Z_{ku}, DFR, and estimated attenuation for melting graupel (D_0 = 3 mm in diameter). Horizontal lines at 4 km and 2 km indicate the top and bottom of the ML. Dry graupel above the ML melts in ML from 4 km to 2 km. Vertical profiles of the estimated attenuation are similar to the theoretical attenuation (Spatt(Ka)-Spatt(Ku)) in Fig. 11 upper axis).

Figure 12 is the same as Fig. 11 but for mixed-phase precipitation; the coexistence of super-cooled raindrops and small ice particles. The fraction of rain amount in the mixed-phase precipitation increases linearly by 0–1 from 2 km to 1 km in altitude. The absorption of ice particles can be neglected at Ka and Ku-bands. The attenuation of the mixed-phase precipitation, therefore, increases with the fraction of the rain amount. The estimated range variation of attenuation correlates well with the theoretical one. Theoretical and estimated attenuation profiles show discontinuous changes at 2 km and 1 km, corresponding to the top and bottom of the ML. Figures 11 and 12 indicate that the attenuation profiles can be a good measure for ML detection in convective precipitation.

In Type 2, clear BB appears in the ML. Here, the ML can be detected from the enhancements in the observed reflectivity. The ML detected from the estimated attenuation can, therefore, be validated by comparing it with the ML detected from the reflectivity enhancements. Because of a large reflectivity enhancement, the values of the smaller weight, w_1 = 0.7, and larger values of w_2 = 0.3 than Type 1 were adopted. In Type 2, Z_m(Ku) increases from the top of the ML, becoming the local maximum, then decreases (Fig. 13). DFR_m starts increasing from the top of the ML, then remains almost constant, indicating a small attenuation in the ML. No apparent peaks are observed in DFR_m. High density and relatively small ice particles could exist above the ML. The local maximum heights of the DFA1 are unrealistically found above the top of the ML, whereas the DFA2 range variations are similar to the reflectivity profiles; the height of the local maximum of Z_m(Ku) and DFA2 are almost consistent (Fig. 13 a, b, c). In Fig. 13d, the local maximum values are found above the top of the ML in DFA2 and DFA1. This peak decreases with the weight of δDFR_s and, therefore, is not actual attenuation.

In Type 3, significant enhancement in both Z_m(Ku) and DFR_m was observed in the ML (Fig. 14), which are typical profiles for the ML of relatively low-density melting snow. The rapid and significant increases indicate the large scattering effects in the ML. The values of the weight, w_1 = 0.5, and values of w_2 = 0.5 were adopted. As in Fig. 13, the locally maximum heights of the DFA1 are unrealistically above the top of the ML, whereas the range variations of the DFA2 are similar to the reflectivity profiles. The additional term DFR_s is useful, specifically for this type. The local maximum heights tend to be slightly lower than those of Z_e(Ku). This could be because the altitudes where the reflectivity is affected by scattering and attenuation are different, specifically near the top of the ML.

5. Attenuation of the melting layer

Attenuation estimation in the ML is essential in high-frequency radar measurements of precipitation. Extensive studies, therefore, have been made using simulations (Matrosov, 2008), dual-Ka-band radars (Nakamura et al., 2018), and dual-frequency radars (Li and Moisseev, 2019). These studies indicate that ML attenuation is larger than the attenuation of resultant rain below the ML. Here, we consider ML attenuation compared with the attenuation in the rain layer below the ML along the radar beam. From Eq. (8), different attenuations between Ka and Ku-bands in the ML (DFA_{ml}) for ranges r_0 and r_1 (Fig. 15) are given by

$$DFA_{ml} = \frac{(DFR_m^1 - DFR_s^1) - (DFR_m^0 - DFR_s^0)}{\Delta r^{ml}}, \quad (14)$$

where DFR_m^1 and DFR_m^0 are the measured DFR at ranges r_1 and r_0, and DFR_s^0 and DFR_s^1 are DFR_s at r_1 and r_0, respectively. Δr^{ml} is $r_1 - r_0$. If the range r_0 is selected as the range where $DFR_m^0 = 0$ and $DFR_s^0 = 0$, such as just above precipitation layer, DFA_{ml} can be determined by only DFR_m^1 and DFR_s^1. DFR_s is smaller than DFA_m in rain; however, exact values of DFR_s^1 are needed to calculate accurate values of DFA_{ml} but is generally unknown. Instead of DFA_{ml}, we consider a ratio of DFA_{ml} to that of the rain layer below the ML. DFA of rain (DFA_{rain}) below the ML for ranges r_1 and r_2 is given by

$$DFA_{rain} = \frac{(DFR_m^2 - DFR_s^2) - (DFR_m^1 - DFR_s^1)}{\Delta r^{rain}}, \tag{15}$$

where, DFR_m^2 and DFR_s^2 are DFR_m and DFR_s at range r_2, respectively. $\triangle r^{rain}$ is $r_2 - r_1$. Set DFR_m^0 and DFR_s^0 to be 0. The ratio of DFA_{ml} to DFA_{rain} (R_{mr}) is expressed as

$$R_{mr} \equiv \frac{DFA_{ml}}{DFA_{rain}} = \frac{(DFR_m^1 - DFR_s^1)}{(DFR_m^2 - DFR_s^2) - (DFR_m^1 - DFR_s^1)} \frac{\Delta r^{rain}}{\Delta r^{ml}}. \tag{16}$$

The scattering effects, DFR_s^1 and DFR_s^2, are calculated from Z_m(Ku) at ranges r_1 and r_2 using Eq. (5), which are relatively good approximations for rain but are incorrect. Incorrect DFR_s values result in erroneous values of the ratio (R_{mr}'). To evaluate the error in the R_{mr}' because of incorrect DFR_s values, ratio of R_{mr}' and R_{mr} true values are calculated using simulations such as

$$\frac{R_{mr}^{\prime}}{R_{mr}} = \frac{(DFA_{ml}/DFA_{rain})^{\prime}}{(DFA_{ml}/DFA_{rain})} \tag{17}$$

where R_{mr} is the ratio of DFA_{ml} to DFA_{rain}, calculated from the true values of DFR_s. R_{mr}' is obtained from erroneous values of DFR_s as $DFR_s^1 = aDFR_s^1$ (true) and $DFR_s^2 = aDFR_s^2$ (true). Parameter a is a proportional coefficient. Figure 16 shows the error ratio given by Eq. (17) as a function of parameter a for various values of DFR_s^1/DFR_m^1. Note that DFR_s^1 is assumed to be the same as DFR_s^2. The larger error appears for larger values of

DFR_s^1/DFR_m^1. Fortunately, δA predominantly determines DFR_m (Le et al., 2016); therefore, the incorrect values of DFR_s are insignificant for estimating R_{mr}.

Figure 17 shows the ratio of the total DFA in the ML to DFA in rain in the range of 1 km, estimated from the DPR data at Shikoku on 7 July, 2018. Note that the attenuation below the ML is not always the attenuation in the resultant rain of the ML because of the slant radar beam and precipitation streak. Further studies are needed by comparisons with other techniques (Awaka et al., 2016, Nakamura et al., 2018, Shusse et al., 2011, 2019).

6. Validation by observations

The attenuation estimation method was examined using the GPM DPR data collected in rain and snow. For attenuating precipitation, such as rain, measured DFR_m tends to increase as the altitude decreases, associated with higher attenuation in the Ka-band than the Ku-band, as mentioned earlier. δA increases monotonically with the radar range and is, therefore, positively correlated to the radar range. High correlations are expected. For dry snow, δA does not exhibit a monotonically increasing tendency because of its low attenuation. Low correlations are expected. High and low values of the correlation coefficients between δA and the radar range are, therefore, expected for attenuating media, such as rain, and small attenuating precipitation, such as dry snow, respectively.

Figure 18 shows frequency histograms of the correlation coefficient for each radar range of 875 m in (a) rain and (b) snow events. Rain data of the DPR observations were selected in the Kanto area, Japan (35.5°N, 139.5°E) on June 5, 2016. Snow data were selected in the Hokuriku region, northern Japan (38.46°N, 136.7 °E) on February 5, 2016. Observed data below ~3 km in altitude were used. The correlation coefficients are higher than 0.95 for most rain events, indicating that attenuating rain exists in the entire range of selected observations. For snow, however, no clear differences exist in the frequencies of the correlation coefficient. indicating that various precipitation, such as dry snow, wet snow, and mixed-phase precipitation of snow and weak rain exist. The figure indicates that the range profiles of the δA obtained using Eq. (8) are good measures to discriminate rain and snow with appropriate threshold values of the correlation coefficient.

7. Conclusions

A new method is proposed to retrieve range variations of DFA from the DFR. The measured DFR is determined from Rayleigh and non-Rayleigh scattering regimes and the different attenuation properties between the two frequencies. The method uses the attenuation effects in the measured DFR_m to derive the DFA range variations. Attenuation properties depend on the type of precipitation and amount of rain/ice drops and, therefore, can be used for hydrometeor classifications. To derive δA, DFR_s is determined from the DFR_s-Z_e relationship (Eq. (5)) and removed from the DFR_m. This relationship depends on precipitation type resulting in an erroneous attenuation estimate. Simulations were used to evaluate the sensitivity of DFR_s-Z_e relations to the estimated attenuation for rain, snow, and mixed-phase precipitation. The results indicate that the estimated attenuation is relatively insensitive to the variability of the relationships.

Sensitivity studies were also conducted for the ML to examine the applicability of the method. In the ML of convective precipitation, no enhanced radar reflectivity is observed, proving the applicability of D-MAD. Here, it is challenging to detect the ML from the reflectivity profiles, but the attenuation profiles can be a good measure for detecting the mixed-phase region in the convective precipitation.

In the ML of stratiform precipitation, the enhanced radar reflectivity by melting particles significantly changes in both DFR_s and δA. The radar ranges, where DFR_m is affected by the scattering and δA, is slightly different, resulting in the insufficient removal by the DFR_s-Z_e relationship, specifically near the top of the ML. For these cases, the DFR_s-Z_e relation was modified by adding a correction term δDFR_s based on the three-parameter Gamma function. The results indicated that the estimated DFA range variations agree with the reflectivity profiles. Furthermore, a technique to estimate the ratio of total attenuations of the ML to attenuation below the ML is proposed based on a similar method to D-MAD.

The method was examined using the GPM DPR data collected in rain and snow events. The correlation coefficients between δA and the radar range were calculated. Frequency histograms of the correlation coefficients show significant differences between rain and snow. The correlation coefficients for most rain events are higher than 0.95, whereas, for snow, no significant differences exist in the correlation coefficient frequencies. The different frequency histograms can be used to discriminate rain and snow with appropriate threshold values of the correlation coefficient.

Note that the method yields range variations of relative values of attenuation and is not intended for attenuation correction but hydrometeor classification. Although the proposed method cannot estimate the exact values of the attenuation amount, it is useful for the GPM DPR mission for accurate rainfall (snow) rate estimates and more accurate precipitation type discrimination by combining it with the conventional method for precipitation type discrimination.

Acknowledgments

This work is partially supported by Japan Aerospace Exploration Agency Precipitation Measuring Mission research program. One of authors (AA) is supported in part by JSPS KAKENHI Grant number JP20K04092. The authors appreciate two anonymous reviewers for useful and detailed comments.

References

Adachi, A., T. Kobayashi, and H. Yamauchi, 2015: Estimation of raindrop size distribution and rainfall rate from polarimetric radar measurements at attenuating frequency based on the self-consistency principle. *J. Meteor. Soc. Japan*, **93**, 359–388.

Akiyama, S., S. Shige, M. K. Yamamoto, and T. Iguchi, 2019: Heavy ice precipitation band in an oceanic extratropical cyclone observed by GPM/DPR: 1. A case study. *Geophys. Res. Lett.*, **46**, 7007–7014.

Awaka, J., M. Le, V. Chandrasekar, N. Yoshida, T. Higashiuwatoko, T. Kubota, and T. Iguchi, 2016: Rain type classification algorithm module for GPM Dual-Frequency Precipitation Radar. *J. Atmos. Oceanic Technol.*, **33**, 1887–1898.

Beard, K. V., and C. Chuang, 1987: A new model for the equilibrium shape of raindrops. *J. Atmos. Sci.*, **44**, 1509–1524.

Chandrasekar, V., R. Keränen, S. Lim, and D. Moisseev, 2013: Recent advances in classification of observations from dual polarization weather radars. *Atmos. Res.,* **119**, 97–111.

Cleveland, W. S., 1979: Robust locally weighted regression and smoothing scatterplots. *J. Amer. Stat. Assoc.*, **74**, 829–836.

Garnett, J. C. M., 1904: Colours in metal glasses and in metallic films. *Philos. Trans. Roy. Soc. London, Ser. A, Math. Phys. Sci.*, **203**, 385–420.

Gunn, K. L. S., and J. S. Marshall, 1958: The distribution with size of aggregate snowflakes. *J. Meteor.*, **15**, 452–461.

Heymsfield, A. J., A. Bansemer, C. Schmitt, C. Twohy, and M. R. Poellot, 2004: Effective ice particle densities from aircraft data. *J. Atmos. Sci.*, **61**, 982–1003.

Hitschfeld, W., and J. Bordan, 1954: Errors inherent in the radar measurement of rainfall at attenuating wavelengths. *J. Meteor.* **11**, 58–67.

Iguchi, T., and R. Meneghini, 1994: Intercomparison of single-frequency methods for retrieving a vertical rain profile from airborne spaceborne radar data. *J. Atmos. Oceanic Technol.,* **11**, 1507–1516.

Joss, J., and A. Waldvogel, 1969: Raindrop size distribution and sampling size errors. *J. Atmos. Sci.*, **26**, 566–569.

Klaassen, W., 1990: Attenuation and reflection of radio waves by a melting layer of precipitation. *IEE Proc., Part H*, **137**, 39–44.

Kobayashi, T., S. Sugimoto, M. Nomura, and A. Adachi, 2015: Radar simulation studies for measurement of precipitation from space-borne radar on GPM. *Extended abstract Conference on Radar Meteor.* Amer. Meteor. Soc.

Kobayashi, T., M. Nomura, S. Sugimoto, A. Adachi, N. Nagumo, and H. Hirakuchi, 2017: Radar simulation studies for hydrometeor classification from range profile of polarimetric radar signatures. *Extended abstract of the 38th Conference on Radar Meteor.* Amer. Meteor. Soc., 1–10. [Available at https://ams.confex.com/ams/38RADAR/meetingapp.cgi/Paper/321041.]

Kobayashi T., M. Nomura, S. Sugimoto, A. Adachi, N. Nagumo, and H. Hirakuchi, 2018: A method for estimate of range variation of attenuation from dual-frequency and dual-polarization radar-validation using scattering database of snow. *Extended abstract of the 10th European Conference on Radar in Meteorology & Hydrology*.

Kouketsu, T., H. Uyeda, T. Ohigashi, M. Oue, H. Takeuchi, T. Shinoda, K. Tsuboki, M. Kubo, and K.-I. Muramoto, 2015: A hydrometeor classification method for X-band polarimetric radar: Construction and validation focusing on solid hydrometeors under moist environments. *J. Atmos. Oceanic Technol.*, **32**, 2052–2074.

Kuo, K.-S., E. A. Smith, Z. Haddad, E. Im, T. Iguchi, and A. Mugnai, 2004: Mathematical-physical framework for retrieval of rain DSD properties from dual-frequency Ku–Ka-band satellite radar. *J. Atmos. Sci*., **61**, 2349–2369.

Le, M., and V. Chandrasekar, 2013: Hydrometeor profile characterization method for dual-frequency precipitation radar onboard the GPM. *IEEE Trans. Geosci. Remote Sens.*, **51**, 3648–3658.

Le, M., V. Chandrasekar, and S. Biswas, 2016: Evaluation and validation of GPM dual-frequency classification module after launch. *J. Atmos. Oceanic Technol*., **33**, 2699–2716.

Li, H., and D. Moisseev, 2019: Melting layer attenuation at Ka- and W- bands as derived from multifrequency radar Doppler spectra observations. *J. Geophys. Res.: Atmos.*, **124**, 9520–9533.

Liao, L., and R. Meneghini, 2005: A study of air/space-borne dual-wavelength radar for estimation of rain profiles. *Adv. Atmos. Sci.*, **22**, 841–851.

Liao, L., and R. Meneghini, 2011: A study on the feasibility of dual-wavelength radar for identification of hydrometeor phases. *J. Appl. Meteor. Climatol.*, **50**, 449–456.

Liao, L., and R. Meneghini, 2019: A modified dual-wavelength technique for Ku- and Ka-band radar rain retrieval. *J. Appl. Meteor. Climatol.*, **58**, 3–18.

Liao, L., R. Meneghini, A. Tokay, and L. F. Bliven, 2016: Retrieval of snow properties for Ku- and Ka-band dual-frequency radar. *J. Appl. Meteor. Climatol.*, **55**, 1845–1858.

Liao, L., R. Meneghini, A. Tokay, and H. Kim, 2020: Assessment of Ku- and Ka-band dual-frequency radar for snow retrieval. *J. Meteor. Soc. Japan*, **98**, 1129–1146.

Marshall, J. S., and W. M. K. Palmer, 1948: The distribution of raindrops with size. *J. Meteor.*, **5**, 165–166.

Matrosov, S. Y., 1998: A dual-wavelength radar method to measure snowfall rate. *J. Appl. Meteor.*, **37**, 1510–1521.

Matrosov, S. Y., A. J. Heymsfield, and Z. Wang, 2005: Dual-frequency radar ratio of nonspherical atmospheric hydrometeors. *Geophys. Res. Lett.*, **32**, L13816, doi:10.1029/2005GL023210.

Matrosov, S. Y., 2008: Assessment of radar signal attenuation caused by the melting hydrometeor layer. *IEEE Trans. Geosci. Remote Sens.*, **46**, 1039–1047.

Matsuo, T., and Y. Sasyo, 1981: Melting of snowflakes below freezing level in the atmosphere. *J. Meteor. Soc. Japan*, **59**, 10–25.

Meneghini, R., and K. Nakamura, 1990: Range profiling of the rain rate by an airborne weather radar. *Remote Sens. Environ.*, **31**, 193–209.

Meneghini, R., H. Kim, L. Liao, J. Kwiatkowski, and T. Iguchi, 2021: Path attenuation estimates for the GPM Dual-Frequency Precipitation Radar (DPR). *J. Meteor. Soc. Japan*, **99**, doi:10.2151/jmsj.2021-010.

Nakamura K., Y. Kaneko, K. Nakagawa, H. Hanado, and M. Nishikawa, 2018: Measurement method for specific attenuation in the melting layer using a dual Ka-band radar system. *IEEE Trans. Geosci. Remote Sens*., **56**, 3511–3519.

Oguchi, T., 1983: Electromagnetic wave propagation and scattering in rain and other hydrometeors. *Proceedings of the IEEE*, **71**, 1029–1078.

Petty, G. W., and W. Huang, 2010: Microwave backscatter and extinction by soft ice spheres and complex snow aggregates. *J. Atmos. Sci*., **67**, 769–787.

Ryzhkov, A., M. Diederich, P. Zhang, and C. Simmer, 2014: Potential utilization of specific attenuation for rainfall estimation, mitigation of partial beam blockage, and radar networking. *J. Atmos. Oceanic Technol.*, **31**, 599–619.

Seto, S., T. Iguchi, R. Meneghini, J. Awaka, T. Kubota, T. Masaki, and N. Takahashi, 2021: The Precipitation rate retrieval algorithms for the GPM Dual-frequency Precipitation Radar., 99, https://doi.org/10.2151/jmsj.2021-011

Shusse, Y., N. Takahashi, K. Nakagawa, S. Satoh, and T. Iguchi, 2011: Polarimetric radar observation of the melting layer in a convective rainfall system during the rainy season over the East China Sea. *J. Appl. Meteor. Climatol*., **50**, 354–367.

Shusse, Y., T. Maesaka, K. Kieda, and K. Iwanami, 2019: Polarimetric radar observation of the melting layer in a winter precipitation system associated with a south-coast cyclone in Japan. *J. Meteor. Soc. Japan*, **97**, 375–385.

Skofronick-Jackson, G., M. Kulie, L. Milani, S. J. Munchak, N. B. Wood, and V. Levizzani, 2019: Satellite estimation of falling snow: A Global Precipitation Measurement (GPM) Core Observatory perspective. *J. Appl. Meteor. Climatol*., **58**, 1429–1448.

Thurai, M., E. Chobanyan, V. N. Bringi, and B. M. Notaroš, 2015: Large raindrops against melting hail: Calculation of specific differential attenuation, phase and reflectivity. *Electronics Letters.* **51**, 1140–1142

Zawadzki, I., W. Szyrmer, C. Bell, and F. Fabry, 2005: Modeling of the melting layer. Part III: The density effect. *J. Atmos. Sci*., **62**, 3705–3723.

List of Figures

Fig. 1 Measured range variations of Z_m(Ka) and Z_m(Ku) for snow and rain events. The range bin resolution is 125 m.

Fig. 2 Simulated Dz versus theoretical values of the δA (solid) for (a) rain where the rain rate varies from 0 to 50 mmh^{-1} (dotted) and (b) melting snow where the water fraction varies from 0 to 1.

Fig. 3 Estimated DFA and theoretical values of the difference of the specific attenuation between Ka and Ku-bands for (a) rain and (b) melting snow shown in Fig.2.

Fig. 4 Simulated DFRs-Z_e(Ku) relationships for (a) rain of various DSD and (b) melting snow of various water fractions (wf). The radar elevation is nadir.

Fig. 5 Range variations of (a) parameter Dz and (b) estimated attenuation and theoretical values of the difference in the specific attenuation between Ka and Ku-bands for rain. Note, DFA is twice the theoretical difference.

Fig. 6 Range variations of (a) parameter Dz and (b) estimated attenuation and theoretical values of the difference in the specific attenuation between Ka and Ku-bands for snow.

Fig. 7 Estimated DFA and theoretical values of the difference in the specific attenuation between Ka and Ku-bands for mixed-phase precipitation.

Fig. 8 (a) Simulated vertical profiles of DFRs and Z_e(Ku) in the ML. The water fraction of snow is 0 at altitude = 2.1 km and 1 at 1.1 km. (b) Range profiles of Z_m(Ka),

Z_m(Ku), and DFR_m (DFR) measured with the GPM at Shikoku, Japan on 7 July, 2018.

Fig. 9 (a) Simulated profiles of DFRs, Dz, apparent reflectivity Z, and DFR(+15) for melting snow. Snow starts melting at an altitude of 2 km and becomes rain at 1 km. (b) The simulated values of Dz and DFA for various weight values. See the text for the meaning of the notations.

Fig. 10 Vertical profiles of Z_m(Ka), Z_m(Ku), DFR, and estimated DFA using DFR_s-Z_e relations by Eq. (5) (DFA1, green) and by Eq. (12) (DFA2, red) for data selected from Type1. Data are selected from the GPM at Shikoku, Japan on 7 July, 2018.

Fig. 11 Simulated vertical profiles of apparent reflectivity Z_{Ka}, Z_{ku}, DFR, estimated DFA, and specific attenuation differences (upper axis) between Ka and Ku-bands for melting graupel. The horizontal lines show the top and bottom of ML.

Fig.12 The same as Fig 11 but for mixed-phase precipitation: coexistence of super-cooled raindrops and small ice particles.

Fig. 13 The same as Fig.10 but for Type 2.

Fig. 14 The same as Fig.10 but for Type 3.

Fig. 15 Schematic figure of DFR profile for estimate total attenuation in ML.

Fig. 16 The ratio given by Eq. (17) as a function of parameter *a* for various values of $DFRs^1/DFR_m^1$.

Fig. 17 The ratio of the total values of DFA in ML to DFA in rain below ML for a range of 1 km, estimated from the DPR data at Shikoku on 7 July, 2018.

Fig. 18 Frequency histograms of the correlation coefficients in the case of (a) rain and (b) snow.

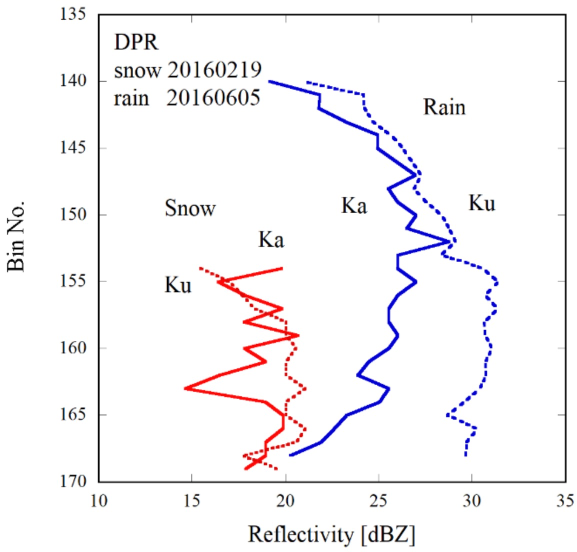

Figure 1 Measured range variations of Z_m(Ka) and Z_m(Ku) for snow and rain events. The range bin resolution is 125 m.

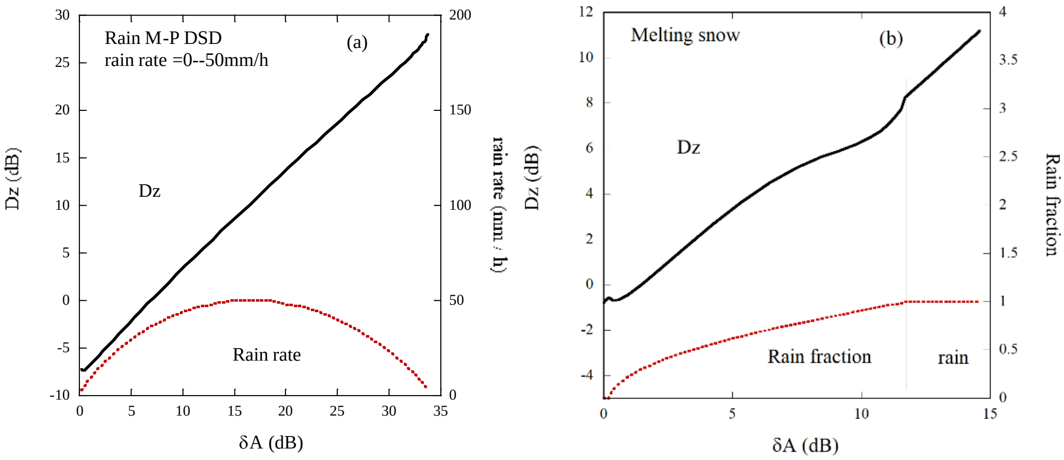

Figure 2 Simulated Dz versus theoretical values of the *δA* (solid) for (a) rain where rain rate varies from 0 to 50 mm/h (dotted) and (b) melting snow where water fraction varies from 0 to 1.

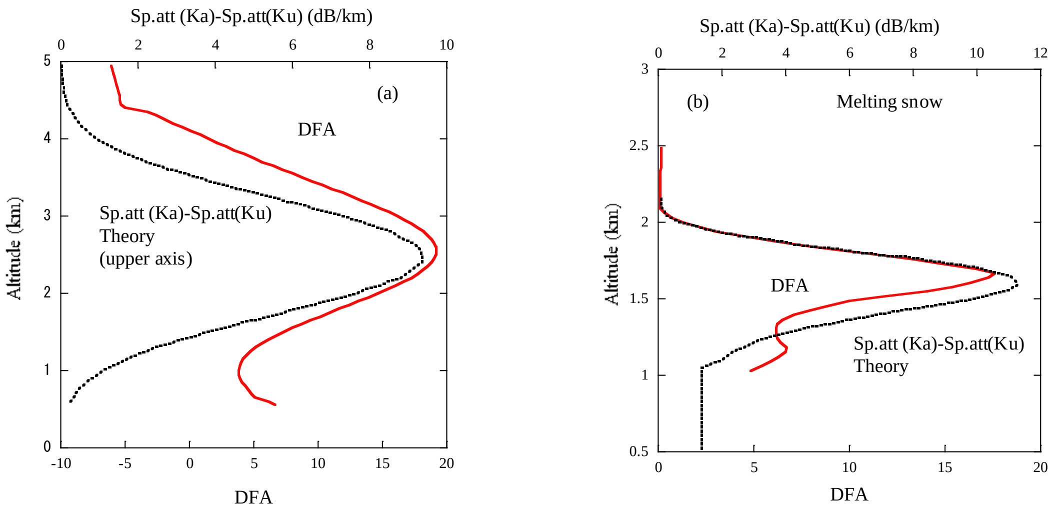

Figure 3 Estimated DFA and theoretical values of the difference of the specific attenuation between Ka and Ku-bands for (a) rain and (b) melting snow shown in Fig.2.

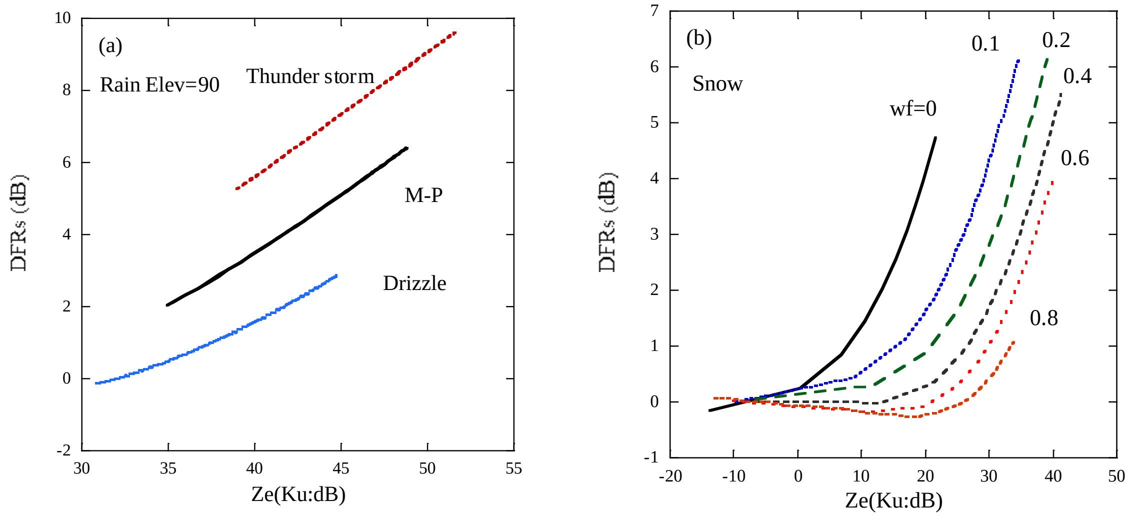

Figure 4 Simulated DFRs- Z_e(Ku) relationships for (a) rain of various DSD and (b) melting snow of various water fractions (wf). The radar elevation is nadir.

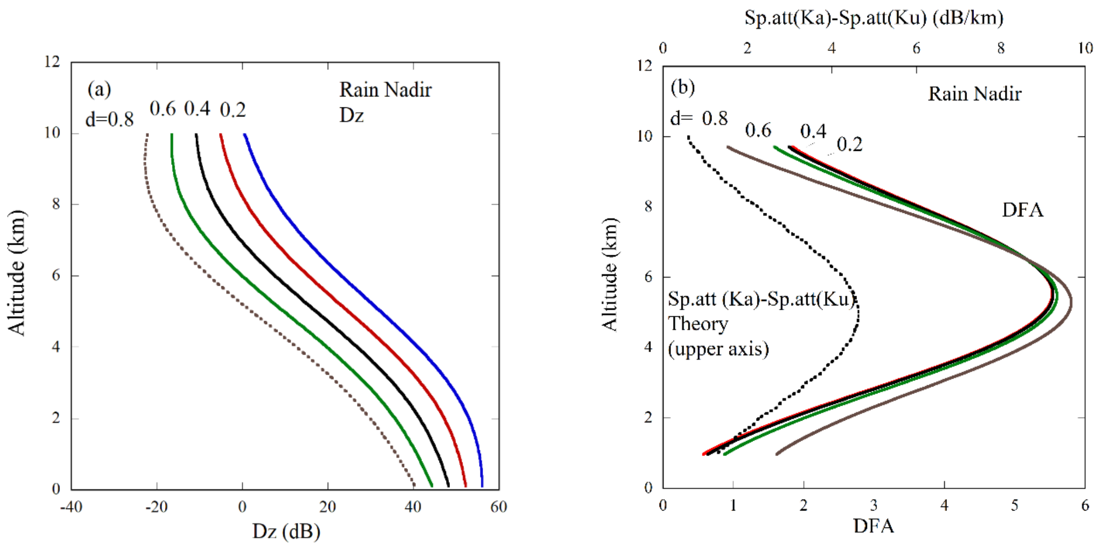

Figure 5 Range variations of (a) parameter Dz and (b) estimated attenuation and theoretical values of the difference in the specific attenuation between Ka and Ku-bands for rain. Note DFA is twice the theoretical values.

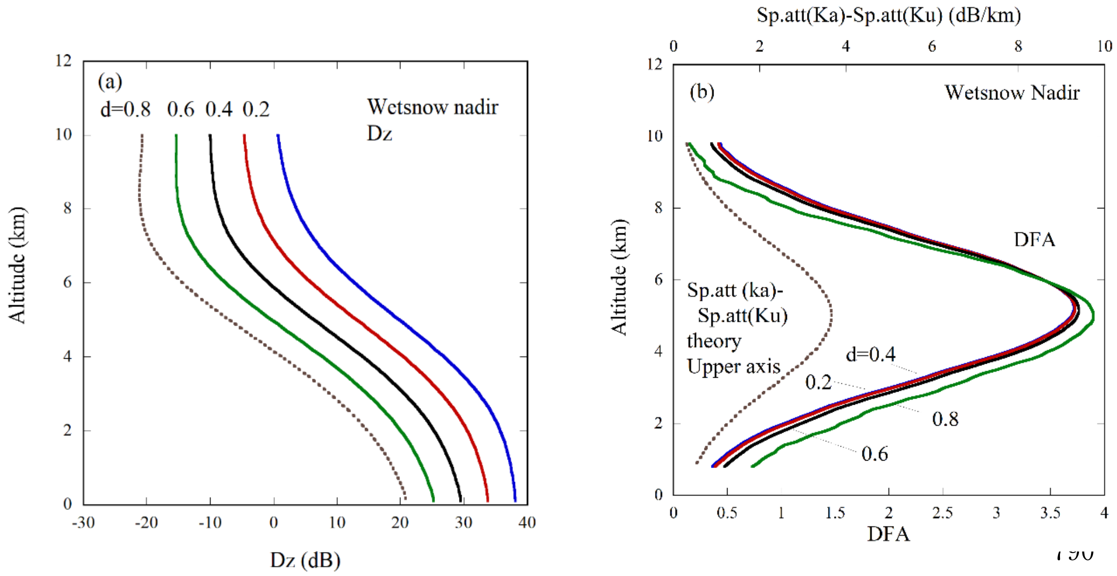

Figure 6 Range variations of (a) parameter Dz and (b) estimated attenuation and theoretical values of the difference in the specific attenuation between Ka and Ku-bands for snow.

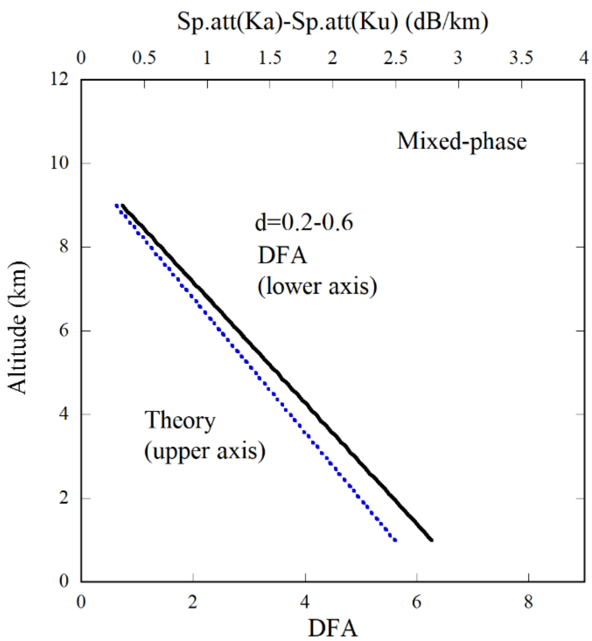

Figure 7 Estimated DFA and theoretical values in the difference of the specific attenuation between Ka and Ku-bands for mixed phase precipitation.

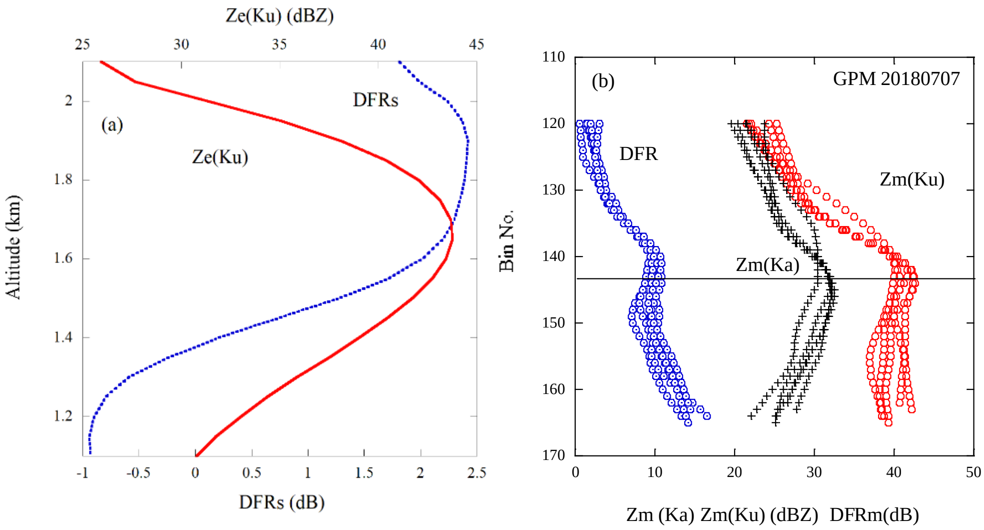

Figure 8 (a) Simulated vertical profiles of DFRs and Ze(Ku) in the ML. The water fraction of snow is 0 at altitude = 2.1 km and 1 at 1.1 km. (b) Range profiles of Z_m(Ka), Z_m(Ku), and DFR_m (DFR) measured with the GPM at Shikoku, Japan on 7 July, 2018 (b).

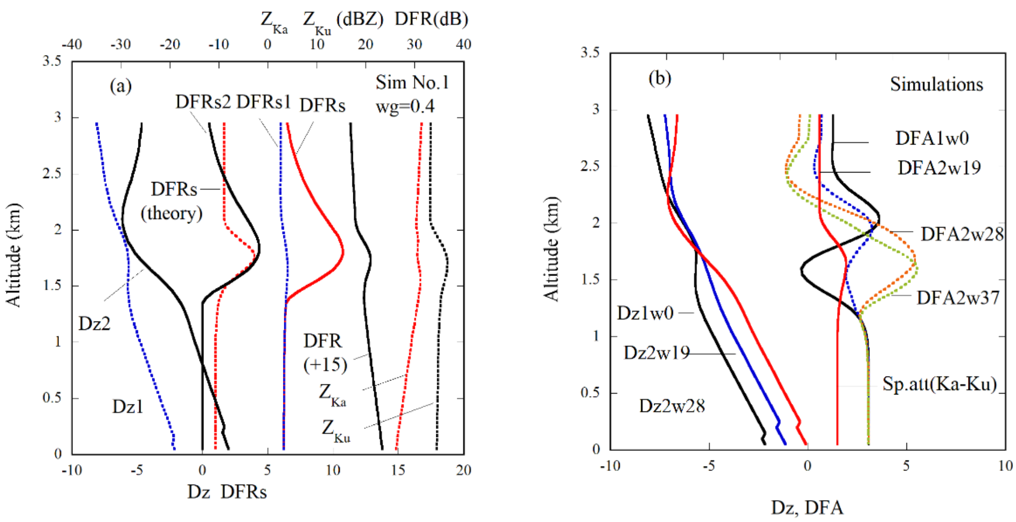

Figure 9 (a) Simulated profiles of DFRs, Dz, apparent reflectivity Z, and DFR(+15dB) for melting snow (a). Snow starts melting at an altitude of 2 km and becomes rain at 1 km. (b) The simulated values of Dz and DFA for various weights values. See the text for the meaning of the notations.

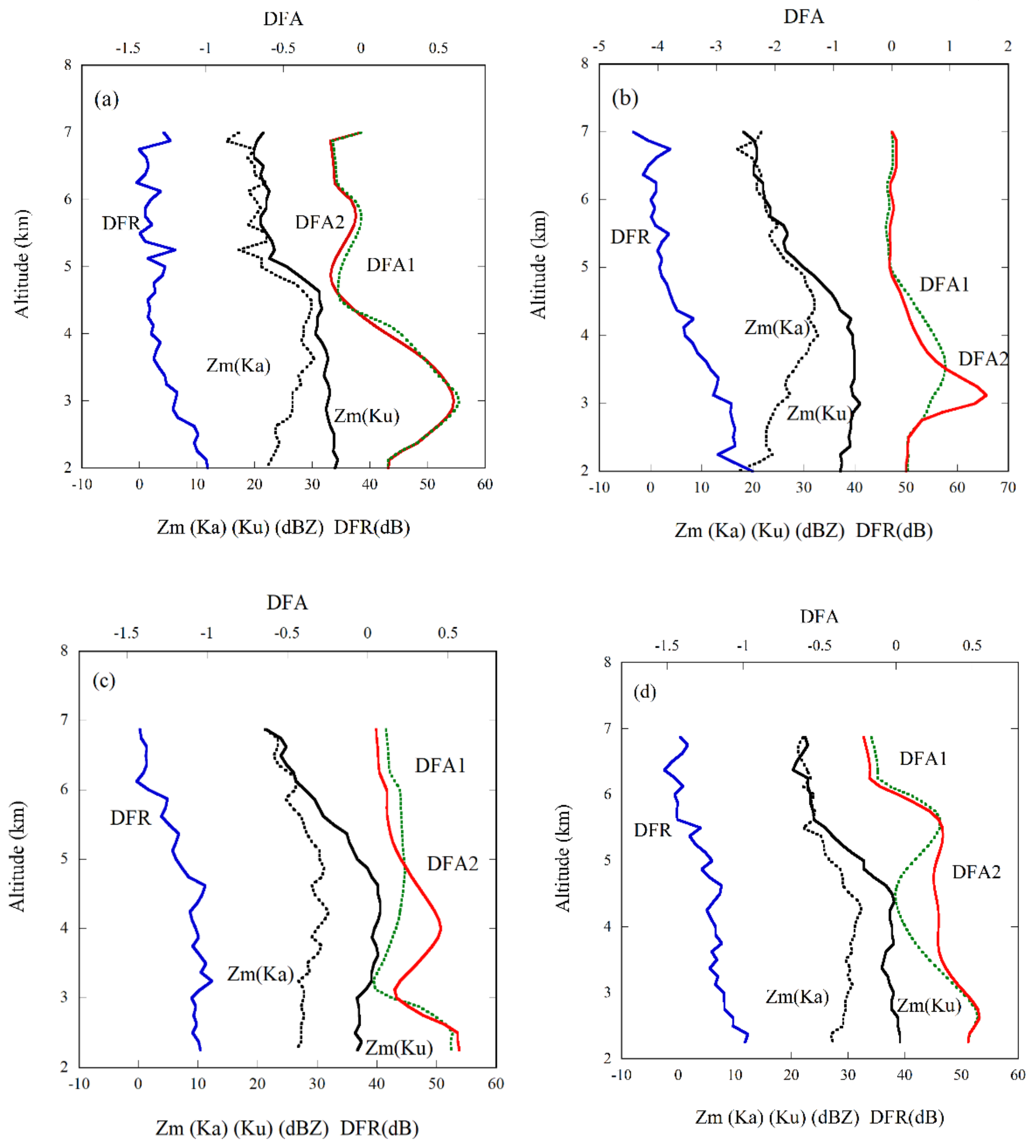

Figure 10 Vertical profiles of Z_m(Ka), Z_m(Ku), DFR and estimated DFA using DFRs-Z_m relations by Eq.(5) (DFA1:green) and by Eq.(12) (DFA2:red) for data selected from Type 1. Data are selected from the GPM measurements at Shikoku, Japan on 7 July, 2018.

.

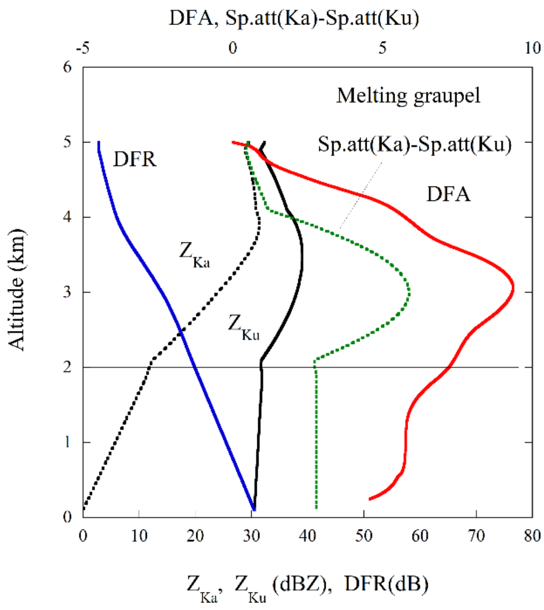

Figure 11 Simulated vertical profiles of Z_{ka}, Z_{ku}, DFR, estimated DFA and specific attenuation difference (upper axis) between Ka and Ku-bands for melting graupel. The horizontal lines show the top and bottom of ML.

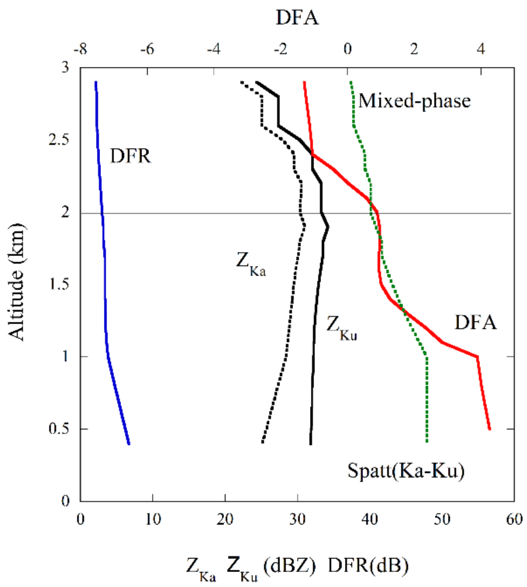

Figure 12 The same as Fig 11, but for mixed-phase precipitation: coexistence of super-cooled raindrops and small ice particles.

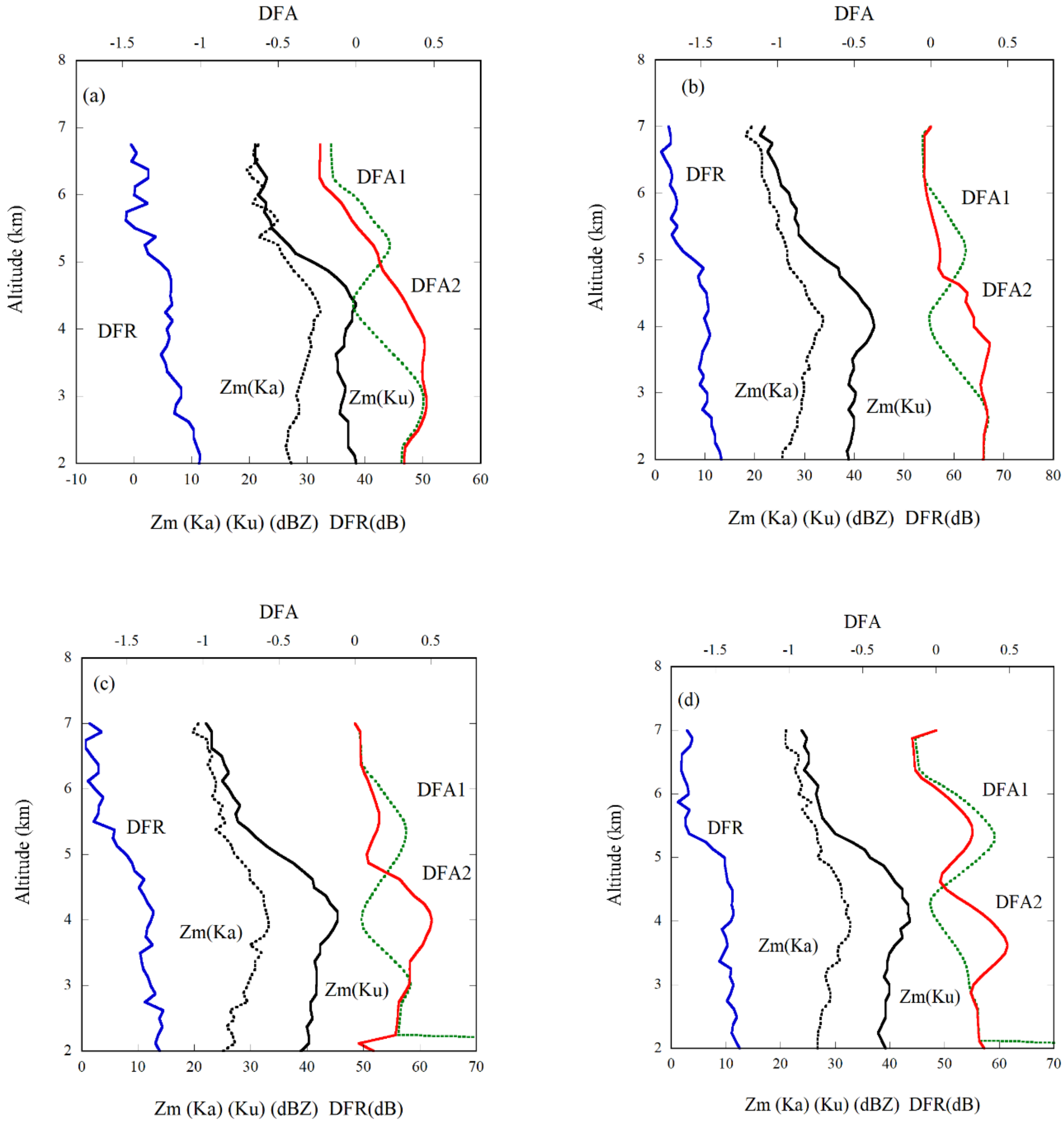

Figure 13 The same as Fig.10 but for Type2.

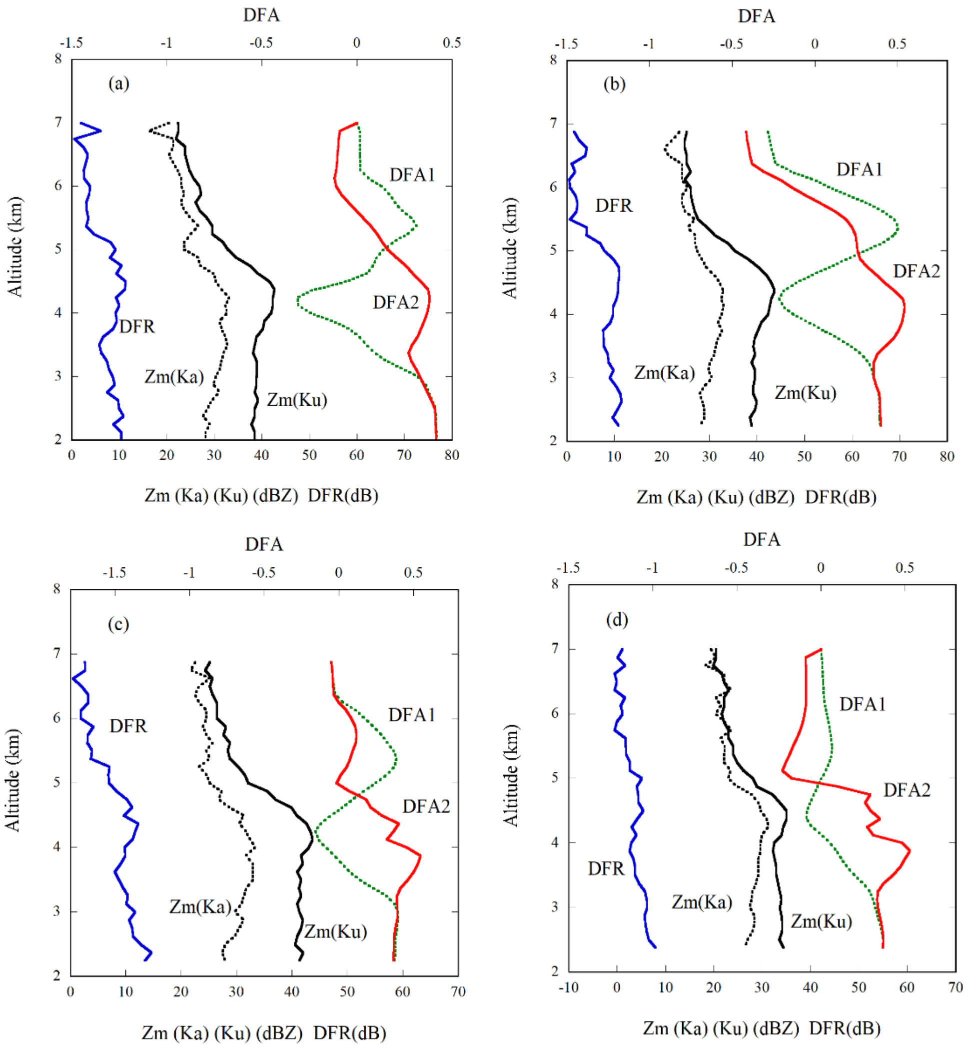

Figure 14 The same as Fig.10, but for Type 3.

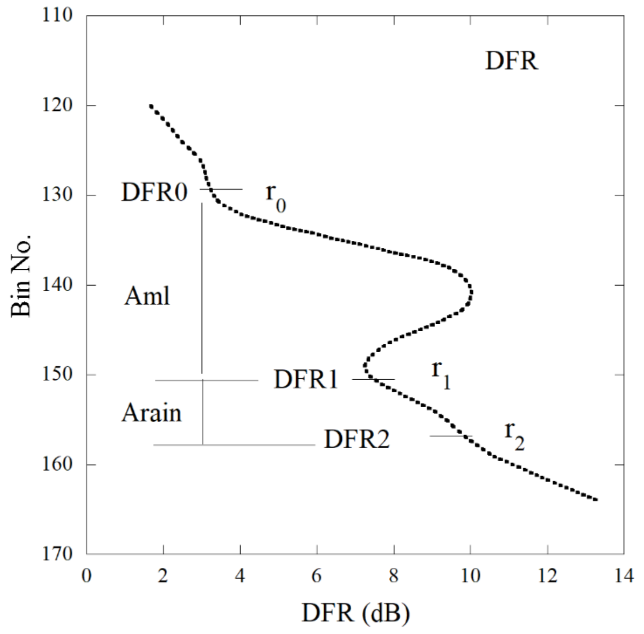

Figure 15 Schematic figure of DFR profile for estimate total attenuation in ML.

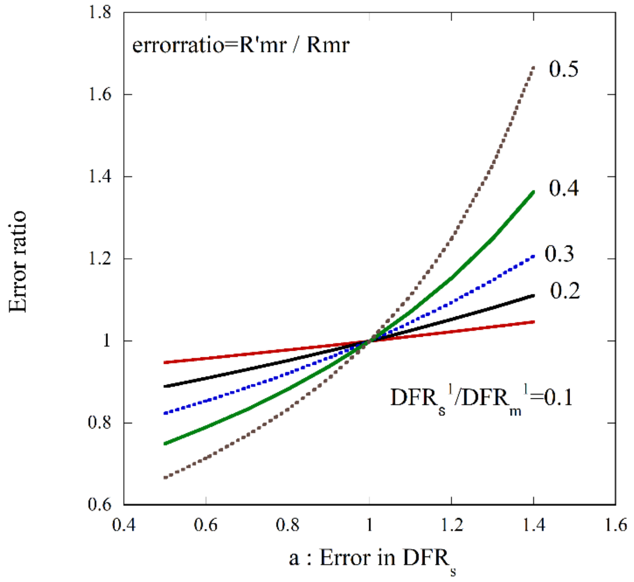

Figure 16 The ratio given by Eq. (17) as a function of parameter *a* for various values of DFR_s^1/DFR_m^1.

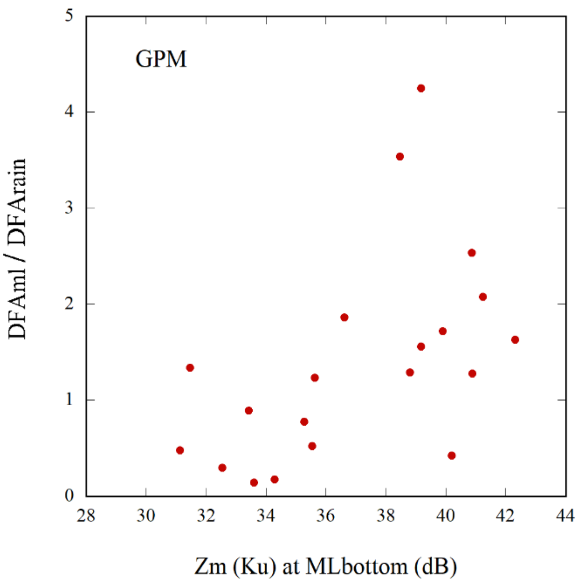

Figure 17 The ratio of the total values of DFA in ML to DFA in rain below ML for range of 1 km estimated from the DPR data at Shikoku on 7 July, 2018.

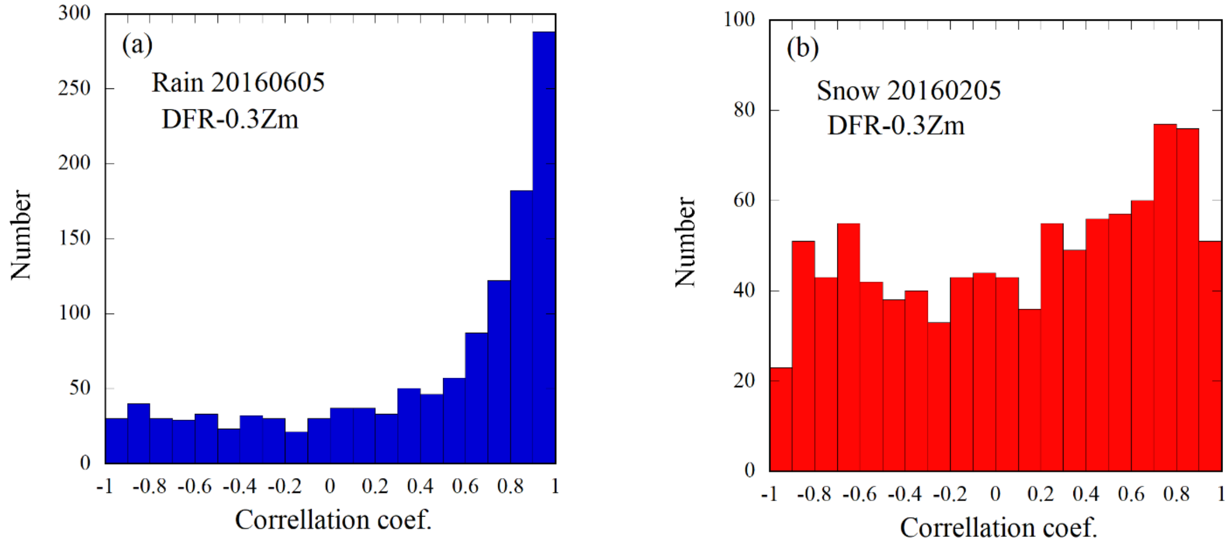

Figure 18 Frequency histograms of the correlation coefficients in the case of (a) rain and (b) snow .